Escaping Compact Object Binaries from Globular Clusters

Annie Csomor

Lund Observatory
Lund University

2022-EXA192

Degree project of 15 higher education credits
June 2022

Supervisor: Abbas Askar

Lund Observatory
Box 43
SE-221 00 Lund
Sweden

Abstract

Since 2015, the LIGO-Virgo-KAGRA scientific collaboration (LVK) has detected gravitational waves from more than 90 merging compact object binaries using ground-based interferometric detectors. Compact objects orbiting in binary systems emit gravitational waves leading to a loss of energy. This results in the decay of the orbit leading to the merger of these inspiralling objects. Around 83 of the merging compact object binaries that have been detected are binary black holes. A couple of binary neutron star mergers and a handful of BH-NS mergers have also been detected. The exact astrophysical origin of these gravitational wave sources is uncertain. The two main formation channels for these compact object binary systems are isolated evolution of massive stars and dynamical formation in dense star clusters. In this thesis project, we explore the latter scenario and investigate compact object binaries that are produced and ejected from globular clusters. We utilise results from around 280 globular cluster simulations to investigate the properties of escaping compact binaries.

We find 8765 escaping binary black holes from the simulated star cluster models. More than 80% of these formed due to dynamical exchange encounters. We find that 40% of the escaping binary black holes from our simulations will merge within the age of the Universe by emitting gravitational wave radiation. We find that initially denser cluster models are more likely to produce more merging binary black holes. Binary black holes that form in exchange encounters inside globular clusters can have component masses larger than 50 $M_\odot$. Dynamical exchange encounters can also produce BBHs with low mass ratios ($\lesssim 0.3$) that are difficult to produce through binary evolution of massive stars. We also identify about 124 BH-NS systems. About 50% of these will merge within the age of the Universe and only less than 10% of these formed in dynamical exchange encounters. We find that merging BH-NS binaries with mass ratio less than 0.1 are more likely to have formed dynamically. In summary, we find that dense clusters can be efficient factories for producing compact object binaries that will merge due to gravitational wave radiation. However, if the initial density is too high, this can lead to the formation of an IMBH which then inhibits the formation of stellar-mass BBHs.

Populärvetenskaplig beskrivning

Stjärnorna som vi ser på natthimlen bor i stjärnhopar med varierande storlek och ålder. De största och äldsta är de så kallade klotformiga stjärnhoparna. Dessa kan innehålla allt från några hundra tusen till flera miljoner stjärnor, varav majoriteten är samlade i en extremt tät kärna i hopens centrum. På grund av den höga densiteten så interagerar dessa stjärnor väldigt frekvent med varandra. Detta gör klotformiga stjärnhopar till de perfekta laboratorierna för att studera det vi kallar den dynamiska evolutionen av astronomiska objekt.

Inom astronomin används ordet dynamik för att beskriva orsakerna till att olika objekt i rymden rör sig. Dynamiska processer styrs av gravitationskraften – en attraktiv kraft som påverkar allt som har massa. Gravitationella interaktioner påverkar stjärnhoparnas struktur genom att tvinga massiva objekt att röra sig mot hopens centrum, och mindre massiva objekt att migrera utåt. Följaktligen är stjärnrester såsom neutronstjärnor och svarta hål väldigt vanliga i hoparnas kärnor. Där kan kompakta binära system i vilka båda komponenterna är neutronstjärnor och/eller svarta hål bildas genom dynamiska interaktioner. Alternativt kan två stjärnor vara bundna till varandra från födseln och sedan bilda binära system av kompakta objekt som en följd av stellär evolution. Två kompakta objekt som kretsar nära varandra i ett binärt system förlorar energi genom att skicka ut gravitationsvågor. Detta resulterar i att omloppsbanan blir mindre och mindre tills de två komponenterna slutligen smälter samman. Sådana händelser är bland de mest energirika i Universum, och ungefär 90 st har upptäckts sedan 2015 med hjälp av markbaserade detektorer.

Syftet med det här projektet är att studera kompakta binära system som har blivit utkastade från sina stjärnhopar genom dynamiska interaktioner, och som kan vara potentiella källor till gravitationsvågor. Mer specifikt så analyserar vi resultaten av detaljerade simuleringar av klotformiga stjärnhopar som genomförts med en av de mest avancerade och funktionsrika koderna som finns tillgängliga idag. Med hjälp av denna kod kan vi följa evolutionen av våra binära system, samt deras påverkan på stjärnhoparna.

Vi undersöker antal, egenskaper och formationshistoria av utkastade kompakta binära system och hur dessa är relaterade till egenskaperna av sina stjärnhopar. Under projektet identifierar vi tusentals system av binära svarta hål, och strax över hundra binära neutronstjärnor från de simulerade stjärnhoparna. Majoriteten av de binära svarta hålen har bildats genom dynamiska interaktioner. Vidare finner vi att de binära system som bildats i simulerade stjärnhopar med högre densitet har större sannolikhet att smälta samman och avge gravitationsvågor inom Universums ålder.

Acknowledgements

Firstly, I would like to express my gratitude to my supervisor, Abbas Askar, for his invaluable guidance and support throughout this project. In addition, I would like to thank Markus Strickert for sharing examples of scripts, which were very helpful for me when getting started with the data processing for my project.

This research has made use of data or software obtained from the Gravitational Wave Open Science Center (gw-openscience.org), a service of LIGO Laboratory, the LIGO Scientific Collaboration, the Virgo Collaboration, and KAGRA. LIGO Laboratory and Advanced LIGO are funded by the United States National Science Foundation (NSF) as well as the Science and Technology Facilities Council (STFC) of the United Kingdom, the Max-Planck-Society (MPS), and the State of Niedersachsen/Germany for support of the construction of Advanced LIGO and construction and operation of the GEO600 detector. Additional support for Advanced LIGO was provided by the Australian Research Council. Virgo is funded, through the European Gravitational Observatory (EGO), by the French Centre National de Recherche Scientifique (CNRS), the Italian Istituto Nazionale di Fisica Nucleare (INFN) and the Dutch Nikhef, with contributions by institutions from Belgium, Germany, Greece, Hungary, Ireland, Japan, Monaco, Poland, Portugal, Spain. The construction and operation of KAGRA are funded by Ministry of Education, Culture, Sports, Science and Technology (MEXT), and Japan Society for the Promotion of Science (JSPS), National Research Foundation (NRF) and Ministry of Science and ICT (MSIT) in Korea, Academia Sinica (AS) and the Ministry of Science and Technology (MoST) in Taiwan.

Furthermore, I would like to thank my friends Ebba Ahlvin and Elsa Nguyen for their constant encouragement. Special thanks to Andreas Evensen for always supporting me and cheering me up; I would not have been able to complete this project without you. I am also incredibly thankful for the support and understanding that my mom, Yvonne Csomor, and my aunt, Maria Möller, have shown me not only throughout this project, but the entirety of my education. Finally, I would like to thank my grandpa, Laszlo Csomor, who sadly did not get to see me finish this project, but who always believed in me, and who would have been prouder and happier than anyone else to see the finished project.

Contents

Chapter 1

Introduction

1.1 Background

Star clusters are gravitationally bound systems of stars sharing a common origin. Thus, stars residing in the same cluster are similar to each other in terms of age, intrinsic properties and metallicity. Furthermore, star clusters can be classified based on e.g. size and structure. For instance, the smallest stellar associations contain only a few tens of stars, while the largest clusters contain up to billions of stars (Karttunen et al., 2017).

This thesis specifically concerns globular clusters (hereafter referred to as GCs), which contain $10^4 - 10^7$ stars, whereof the majority are concentrated in a central core with a radius of $0.3 - 10$ pc surrounded by an extended envelope that may be $10 - 100$ times larger (Karttunen et al., 2017). The high central density makes GCs highly suitable as laboratories for the investigation of dynamical interactions between astronomical bodies. Furthermore, GCs offer many opportunities regarding the study of e.g. cluster evolution, dynamics and the formation and evolution of exotic objects such as black holes (BHs) and compact object binary systems (Davies, 2013). Throughout this thesis, the latter refers to binaries where both components are either a BH or a neutron star (NS). Merging compact object binary systems are sources of gravitational waves and dynamical encounters in GCs can be conducive to their formation (Portegies Zwart & McMillan, 2000; Rodriguez et al., 2016). Our focus is on using results from simulated GCs to look for such compact binaries that escape from GCs. We investigate the numbers and properties of these escaping binaries and how they correlate with the properties of their respective birth clusters.

GCs are discussed in greater detail in Section 1.2, which starts with a description of their structure and characteristic properties. Next, the formation, properties and importance of compact binaries are described in Section 1.3, where we also present recent LIGO-Vigro-KAGRA (LVK) detections of merging compact binaries. Finally, the physical importance and aim of this project is presented in Section 1.4.

1.2 Globular Clusters

GCs are some of the oldest structures in the Universe which orbit around their host galaxies. Typical GCs in the Milky Way are roughly 13 billion years (Gyr) old. For comparison, the Universe is approximately 13.8 Gyr old (Karttunen et al., 2017). However, massive star clusters with ages of up to 3 Gyr old have been observed in e.g. the small and large Magellanic clouds, as well as star forming regions in merging galaxies. Furthermore, there are about $150 - 200$ GCs spherically distributed across the Milky Way, while some galaxies have been found to host more than 10 000 GCs (Harris et al., 2013). Thus, GCs of widely varying ages are seemingly common in our Universe (Benacquista & Downing, 2013).

As already mentioned, GCs are also some of the largest star clusters, containing up to 10^7 stars. These are mainly Population II stars with low metallicity distributed in such a way that the majority of the stars form a central core with densities up to 10^6 $M_\odot$ pc^{-3} (Karttunen et al., 2017), while the stellar density in the Solar neighborhood is ~ 0.1 pc^{-3} (Benacquista & Downing, 2013).

1.2.1 Structure and Properties

In terms of structure, GCs can be seen as roughly spherical N-body systems consisting of a self-gravitating, extremely dense central core surrounded by a less self-gravitating, low-density halo. This can be described in more depth using the different radii presented in Table 1.1, (Benacquista & Downing, 2013).

Table 1.1: Characteristic radii used to describe the structure of GCs.

Notation	Name	Definition
r_c	Core radius	Radius at which the surface density is half of the central value
r_hm	Half-mass radius	Radius containing half of the mass of the system
r_hl	Half-luminosity radius	Radius enclosing half of the light emitted by the cluster
r_t	Tidal radius	Radius at which the gravitational field of the galaxy dominates over the self-gravity of the cluster

The evolution of GCs is driven by gravitational encounters, and can be further characterized using a few important timescales. Since gravity has a long range, the cumulative effect of interactions with distant bodies significantly impacts the motion of a single star. Eventually, the star reaches relaxation, that is, it has been subjected to enough gravitational encounters to completely "forget" its initial orbit (Mapelli, 2017c). Thus,

we define the relaxation time, $t_{\rm rlx}$, as the time time needed for a cluster to relax. The relaxation time is related to the number of stars in the cluster as follows (Binney & Tremaine, 2008; Spitzer, 1987),

$$t_{\rm rlx} \propto \frac{N}{\ln(N)} t_{\rm cr}. \tag{1.1}$$

Here, $t_{\rm cr}$ is the crossing time of the system, defined as the time needed for a star with velocity dispersion v to cross some characteristic radius R (e.g. one of the radii presented in Table 1.1) of the cluster (Benacquista & Downing, 2013),

$$t_{\rm cr} \sim \frac{R}{v}. \tag{1.2}$$

For typical GCs, the relaxation time lies within $0.1 - 1$ Gyr, while the average age is greater than 10 Gyr. Thus, we expect GCs to be relaxed. However, due to the difference in density between the core and halo, this is not necessarily true for the entire cluster. Rather, $t_{\rm rlx}$ must be seen as a function of location within a cluster, and can vary significantly within the cluster. Consequently, a cluster might have a relaxed core, but an un-relaxed halo (Benacquista & Downing, 2013; Davies, 2013). Furthermore, a system is considered to be collisional if its relaxation timescale is short with respect to its lifetime. By this definition, GCs are collisional, and we need to consider timescales larger than $t_{\rm rlx}$ in order to describe the evolution of the system (Mapelli, 2017c).

1.2.2 Dynamical Evolution

This subsection concerns the different evolutionary states of GCs, starting with the formation of the cluster. There are indications that the entire stellar population of a GC forms at the same time as a result of a collapse of a single giant molecular cloud. Supporting evidence include the fact that the stars residing within a single cluster all tend to have similar metallicities. In addition, the stellar population follows a common main sequence, main sequence turnoff, horizontal and giant branch. These similarities, in combination with a small age spread within a population, imply the common origin of the stellar population (Benacquista & Downing, 2013).

The initial mass distribution for the stellar population is given by the so-called initial mass function (IMF), which is a power law on the form (Benacquista & Downing, 2013)

$$\frac{dN}{dM} \propto M^{-\alpha_i}, \tag{1.3}$$

where N is the number of stars, M the stellar mass, and the dimensionless α_i can assume different values for different mass ranges. The IMF favours low-mass stars, meaning that massive stellar remnants such as neutron stars (NSs) and BHs will be rare due to the low number of stars with sufficient mass to evolve into such remnants (Benacquista & Downing, 2013). Taking an α_i value of 2.3 for stars above 0.5 $M_\odot$ (Kroupa, 2001), about 2 to 4 in every 1000 stars evolve into a BH or a NS.

Once formed, GCs evolve through dynamical two-body interactions. Close gravitational encounters between two stars, and the resulting exchange of energy, cause local changes to the stellar orbits and velocities (Mapelli, 2017b). This deflection is related to the separation between the stars in such a way that close encounters cause large deflections, while distant encounters cause comparably small deflections. On the other hand, distant encounters have a greater impact on the cluster evolution than close ones. This is due to the fact that distant encounters occur much more frequently, and therefore, the accumulated effect of many such encounters dominates over the effect of the less frequent close encounters. The timescale on which this happens is the two-body relaxation timescale (Chandrasekhar, 1942; Hénon, 2011; Spitzer, 1987).

Mass Segregation

The accumulated effects of the two-body interactions described above has two main consequences. Stars gain energy and may be ejected from the cluster in a process referred to as evaporation, which occurs if the velocity of the star exceeds the escape velocity $v_{\rm esc}$ of the cluster. The escape velocity is related to the gravitational potential ϕ of the cluster by (Spitzer & Harm, 1958)

$$\frac{1}{2}v_{\rm esc}^2 = |\phi|. \tag{1.4}$$

GCs also lose stars due the tidal field of the cluster's host galaxy, which is not discussed in detail in this thesis. Furthermore, dynamical interactions drive the stars towards equipartition, meaning that the total kinetic energy available in a local part of the cluster is shared equally among the stars. Consequently, more massive objects sink towards the center of the cluster while less massive ones migrate outwards into the cluster halo after gaining kinetic energy (Davies, 2013). This process is known as *mass segregation*, and proceeds on timescales $t_{\rm ms}$ given by (Benacquista & Downing, 2013)

$$t_{\rm ms} \propto \frac{m_i}{\langle m \rangle}, \tag{1.5}$$

where m_i is the mass of a specific component and $\langle m \rangle$ is the average mass. Since stars lose mass as they evolve, and high-mass stars evolve quicker than low-mass ones, compact stellar remnants such as NSs and BHs quickly become the most massive objects in GCs. Thus, these objects migrate inwards and are very likely to be found in the central parts of GCs (Benacquista & Downing, 2013).

Instability and Core Collapse

As the core density increases through mass segregation, so does the rate of dynamical interactions in the core. Hence, two-body relaxation and evaporation of energetic stars transport energy from the core to the halo of the cluster. High-velocity stars move out of the cluster core, which results in reduced kinetic energy in the core. This, in turn, causes the core to contract, and thereby become denser. Furthermore, higher core

density leads to shorter two-body relaxation times. Hence, stars exchange more energy, meaning that the kinetic energy of stars in the core is increased. However, these energetic stars evaporate to the halo causing the core to contract further, formally towards a singularity. These processes are referred to as the *gravothermal catastrophe*, and the subsequent *core collapse* (Benacquista & Downing, 2013).

However, observed clusters do not continue collapsing, meaning that there must be some process that halts core collapse. This can be achieved through the presence of binary systems in the core. Stars gravitationally scattering off these binaries gain kinetic energy while the binary loses binding energy in a process known as *binary burning* (Cohn & Hut, 1984; Heggie & Hut, 2003). As a result of this energy transfer, the core will return to equilibrium (Benacquista & Downing, 2013). Therefore, energy generation by binaries in the cores of GCs plays an important role in their evolution.

1.3 Compact Objects

1.3.1 Compact Object Binaries

In this subsection, the two main formation channels of compact binaries are described. Firstly, we have *original* binaries, which are formed as a result of stellar evolution of a binary system comprising massive stars that are bound together since birth. If the two components are sufficiently separated, they will not interfere with each other's evolution, meaning that we can consider them to be two separate systems evolving independently. However, if the separation is small, the stars may interact, which could alter the evolution of the stars as well as the orbit of the binary. Assuming that both stars start in the main sequence, the gravitational potential of the binary can be described by the Roche model, in which each star dominates the gravitational potential inside its own region known as a Roche lobe. The two Roche lobes are connected, and together they form a figure-eight like shape. If either star fills its Roche lobe, matter starts flowing from that star to the other one through the point connecting the two Roche lobes. This process, known as Roche lobe overflow, causes the evolution of the components to proceed in a different way compared to that of isolated stars. As a result, the system may evolve into a compact binary (Hurley et al., 2002; Mapelli, 2021).

Alternatively, frequent gravitational encounters in dense GC cores could lead to the formation of binary systems. Such systems are referred to as *exchanged* binaries. This could occur through single-single interactions, where two objects passing sufficiently close to each other can become tidally locked and form a binary (Benacquista & Downing, 2013; Davies, 2013). Similarly, three-body interactions could result in the least massive body gaining a significant amount of energy, leaving the two more massive bodies to form a binary (Davies, 2013; Mapelli, 2021).

Compact binaries may also be involved in binary-single interactions, which differ from three-body interactions since two of the components are already bound before the interaction (Benacquista & Downing, 2013). The outcome of these encounters depends on whether the binding energy of the binary relative to the kinetic energy of the single star. We define *hard* and *soft* binaries as binaries whose binding energies are higher and lower, respectively, than the average kinetic energy of a star in the cluster (Heggie, 1975; Hills, 1975; Mapelli, 2017a).

Three-body interactions cause soft binaries to be further softened and dissolve. On the other hand, fly-by interactions between a single star and a hard binary tends to harden the binary, either by decreasing its semi-major axis, or by changing its mass. Alternatively, an exchange where the single star replaces one of the binary components can take place. This is favoured in interactions where the single mass is greater than the mass of one of the binary components, meaning that the binding energy of the new binary is increased with respect to the old one (Mapelli, 2017a). During these binary-single encounters, two stars may also pass sufficiently close to become captured by each others tidal field and form a tight binary (Davies, 2013).

1.3.2 Black Hole Subclusters and IMBHs

Forming compact binaries is beneficial for the retention of BHs and NSs in the cluster. Mass segregation causes these objects to sink towards the cluster center, and if the BH population is significant, a BH subcluster (BHS) is formed. Inside this subcluster, binary BHs (BBHs) are formed due to interactions. Consequently, BBHs and BHs participate in binary-single interactions, causing the ejection of BHs from the BHS into the halo of the GC. These BHs then migrate towards the central BHS again while depositing energy into the cluster, causing the cluster to expand. Thus, the BHS is of importance for the dynamical evolution of the entire cluster (Davies, 2013).

Instead of a central BHS, the GC could potentially host a central intermediate-mass black hole (IMBH). These are BHs in the mass range of $10^2 - 10^5$ $M_\odot$, which places them between stellar mass BHs and supermassive BHs in terms of mass. IMBHs were purely theorized and subject to much uncertainty until 2019, when the LIGO-Virgo-KAGRA (LVK) collaboration detected a merging BBH where the components had masses if 66 and 85 $M_\odot$, respectively (Abbott et al., 2020). There are two main formation channels for IMBHs, which are referred to as the *fast* and *slow* scenarios. In the fast scenario, runaway mergers between massive MS stars may accumulate to form an IMBH. Similarly, mergers between stellar-mass BHs and massive stars could also lead to the formation of an IMBH. This ocurrs in GC models with central densities $\gtrsim 10^6$ $M_\odot pc^{-3}$ The alternative, slow, formation channel involves gradual build up of the mass of a stellar-mass BH through mergers with stars and accretion in binary systems (Giersz et al., 2015; Askar et al., 2021).

1.3.3 Gravitational Wave Detections

Dynamical interactions may also result in the ejection of objects, including compact binaries, from GCs. Ejected binaries may then inspiral and merge through the emission of gravitational waves. The time, t_{GW}, needed for this to happen is calculated as follows (Peters, 1964; Di Carlo et al., 2019),

$$t_{GW} = \frac{5}{256} \frac{c^5 a^4 (1-e^2)^{7/2}}{G^3 m_1 m_2 (m_1+m_2)}, \tag{1.6}$$

where c is the speed of light, G is the gravitational constant, a and e are the semi-major axis and eccentricity, respectively, of the binary, and m_1 and m_2 are the masses of the two binary components. At the point of writing this thesis, about 90 such merger events have been detected by the LVK collaboration (Abbott et al., 2021). About 83 of these are BBH mergers, two are NS-NS mergers, and about five are most likely BH-NS mergers.

1.4 Physical Importance and Aim

For this project, we analyzed results of about 280 numerical simulations of GCs in order to investigate escaping compact binaries that can be potential sources of gravitational waves, with specific focus on the merger time and properties of these binaries. Furthermore, we focus on the number and properties of BBHs and BH-NSs that are produced either through dynamical exchange interactions or through the evolution of massive stars that were initially in binary systems. The masses and mass ratio distribution of the merging compact object binary components are compared with LVK detections to see if we can provide any constraints on their astrophysical origin.

Additionally, we look at how initial GC properties effect the properties of escaping binaries and whether initial cluster mass and density has an influence on the properties of escaping compact object binaries (Hong et al., 2018, 2020).

Chapter 2

Method

The results presented in this thesis were generated based on simulation output data from the MOCCA[1] code, which is used to simulate the evolution of realistically sized star clusters. Section 2.1 is dedicated to introducing the MOCCA code, with specific focus on Test Survey 2 (see subsection 2.1.1). Here, details of the initial conditions used for the simulations, as well as the output files, are described. Finally, section 2.2 describes the scripts used to extract the data of interest and generate our results.

2.1 The MOCCA Code for Simulating Star Clusters

MOCCA is a state-of-the-art code that can simulate the evolution of realistic star clusters (Hypki & Giersz, 2013; Giersz et al., 2013). It accounts for all the important physical processes involved in the evolution of a star cluster and provides detailed output for cluster properties and the dynamical history of each star in the cluster. MOCCA combines the particle based approach of direct N-body methods with the Monte Carlo algorithm for treating relaxation that was developed by Hénon (1971) and subsequently improved by Stodolkiewicz (1986) and Giersz (2006). This method uses a statistical approach for approximating the effect of 2-body relaxation in spherically symmetric star clusters without having to directly integrate orbits. As a result, it is significantly faster than direct N-body codes and can compute the evolution of a globular cluster with up to a million stars within a few CPU-days to a week. The cluster models are typically initialized using a King (1966) model with all stars at zero-age main sequence.

For stellar and binary evolution, the current version of the MOCCA code uses prescriptions from an updated version of the population synthesis codes SSE and BSE (Hurley et al., 2000, 2002; Kamlah et al., 2022). For computing the outcome of close binary-single and binary-binary encounters, MOCCA utilizes the small N-body scattering code called *fewbody* (Fregeau et al., 2004). These close encounters are particularly important for the dynamical formation of close binary systems. Additionally, MOCCA also

[1] which stands for MOnte Carlo Cluster simulAtor

incorporates a realistic treatment of escape processes in tidally limited clusters using Fukushige & Heggie (2000). The details of all the features in the MOCCA code version which was used to simulate the models investigated in this thesis have been described in Hypki et al. (2022) and Maliszewski et al. (2021).

Results from MOCCA have been tested against globular cluster models containing up to a million stars that were simulated using direct N-body codes (Wang et al., 2016; Madrid et al., 2017). It has become evident that the results of the two types of simulation have shown great agreement in terms of cluster parameters and properties and numbers of specific stars (see Askar et al. (2017) and references therein). However, while the two approaches give equally as detailed outputs, MOCCA is much faster than N-body codes for the same number of particles in the considered system (Hypki & Giersz, 2013). Therefore, it is well suited for simulating a large number of globular cluster models to probe how initial cluster properties can influence cluster evolution and the production of exotic stellar systems and binaries.

2.1.1 Test Survey 2

For this particular thesis, we use data from the MOCCA-Survey Database II (Maliszewski et al., 2021), which contains data for over 250 simulations with different initial conditions. MOCCA-Survey Database II is an upgraded version of the earlier MOCCA-Survey Database I (see Askar et al. (2017)). The initial conditions used in MOCCA-Survey Database II were chosen in order to investigate the dynamical mixing between two stellar populations with central densities as high as $\rho_c \sim 10^7$ $M_\odot pc^{-3}$ (Maliszewski et al., 2021). A summary of the initial parameters can be found in Table 2.1.

The initial conditions are generated from the `Mcluster code` (Küpper et al., 2011; Kamlah et al., 2022). Most models have initial binary fractions $f_b = 0.95$, although a few models also have $f_b = 0,\ 0.1,\ 0.12,\ 0.146,\ 0.63$ instead. `N` represents the total number of objects (where an object can be either a binary or a single star). The concentration parameter W_0 is the King's concentration parameter defined as $W_0 = \log(r_t/r_c)$, where r_t is the tidal radius (`rbar`) and r_c is the core radius (Peterson & King, 1975). The IMF is given by Kroupa (2001), and the upper limit of the mass function is given by the `mup` parameter (which is set to either 50 $M_\odot$ or 150 $M_\odot$) and the lower limit is 0.08 $M_\odot$. Finally, `rh_mcl` is the initial half-mass radius, and the concentration parameter `conc_pop` gives the ratio $r_{\mathrm{h,mcl,i}}/r_{\mathrm{h,mcl,1}}$ between population i and the first population.

Table 2.1: Initial parameters used in MOCCA test survey II.

Parameter	Initial Value		
`N`	$4 \cdot 10^5$; $2 \cdot 10^5$	$4 \cdot 10^5$; $4 \cdot 10^5$	$4 \cdot 10^5$; $6 \cdot 10^5$
W_0	6.0; 8.0	6.0; 8.0	6.0; 8.0
`mup`	150.0; 50.0	150.0; 50.0	150.0; 50.0
`rbar`	60.0; 120.0	60.0; 120.0	60.0; 120.0
`rh_mcl`	0.6; 1.2; 2.0; 4.0; 6.0	0.6; 1.2; 2.0; 4.0; 6.0	0.6; 1.2; 2.0; 4.0; 6.0
`conc_pop`	0.1; 0.2; 0.5; 1.0; 1.5	0.1; 0.5; 1.0; 1.5	0.1; 0.2; 0.5; 1.0; 1.5

For the `N`, W_0 and `mup` parameters, there are two values per column. This is because the MOCCA version that was used in this project allows the user to include two initially distinct stellar populations in the cluster initial model (see Hypki et al. (2022) for details). The two `N` values, for example, are the initial number of objects in each of the two populations. The first of these populations always has $W_0 = 6.0$ and `mup`$= 150.0$, while the second population can have either $W_0 = 6.0$ or $W_0 = 8.0$, and either `mup`$= 150.0$ or `mup`$= 50.0$. Furthermore, the initial values for `rbar`, `rh_mcl` and `conc_pop` are then varied for each simulation.

Compared to MOCCA-Survey Database I (see Askar et al. (2017)), several upgrades to prescriptions governing the stellar evolution of massive stars were made to the MOCCA code that was used to produce MOCCA-Survey Database II (Maliszewski et al., 2021) models. This includes metallicity dependent stellar winds, pair instability supernovae and improved determination of BH/NS star masses and natal kick (see Kamlah et al., 2022, and references therein). The maximum BH and NS mass formed via stellar evolution in these simulations is about 45 $M_\odot$ and 3 $M_\odot$ respectively.

2.2 Simulation Data and Analysis

The MOCCA code gives a variety of output files for each simulated cluster model. The ones of interest for this project are the `escape.dat` and `system.dat` files. For each model, the `escape.dat` contains properties such as the time of escape, mass and ID number of each escaping object, semi-major axis and eccentricity for escaping binaries, at the time of escape. Meanwhile, the `system.dat` file contains cluster properties, such as total cluster mass and density, the various radii mentioned in Table 1.1, number of single BHs and BBHs and the maximum BH mass, throughout the 15 Gyr during which MOCCA evolves the cluster.

In order to extract the data deemed necessary, we use `awk` scripts, which we pipe through the `subprocess` package in Python. This was done firstly in order to create a file containing escaper and cluster properties at the time of escape, using the script that can be found in Appendix A. In the scripts, we have filtered out everything that is not

a BBH, BH-NS, NSNS, white dwarf (WD) binary, WD-NS or WD-BH, and matched the escape time from `escape.dat` with the time column in `system.dat`. The resulting file had one line for each escaping binary, containing all relevant properties at the time of escape.

Using similar `awk` scripts, cluster properties at 0 Gyr and 12 Gyr were extracted. By using additional `awk` to extract and combine data from these files and the one described in the previous paragraph, a variety of files could be obtained, which allowed for the investigations presented in Chapter 3.

Chapter 3

Results

This chapter is dedicated to the presentation and discussion of the key results from this project. Firstly, in Section 3.1, we give an overview of the numbers and formation channels of the escaping binaries. Next examine some intrinsic properties of BBHs and BH-NSs in Sections 3.2 and 3.3, respectively. Finally, we correlate the number, properties and evolutionary history of these binary systems with the initial properties of their birth clusters, which can be seen in Section 3.4.

3.1 Overview of Escaping Binaries

All MOCCA-Survey Database II cluster models produced a total of 33086 escaping binaries of stellar remnants (i.e. BHs, NSs and WDs). Table 3.1 gives an overview of the types (BBH, BH-NS, NS-NS, WD-WD, WD-NS and WD-BH) of the produced escaping binaries, as well as their formation channels. As can be seen, the majority of the produced escapers are binaries in which at least one component is a white dwarf. The second largest group of escapers are the BBHs. Out of these, 26% were formed originally, and 74% through exchange.

Table 3.1: Numbers of escaping binaries produced by the MOCCA-Survey Database II cluster models, as organized by binary type and formation channel. For each binary type, the total number of produced escapers are given, along with the the numbers (and percent) of these that were formed originally and through exchange encounters.

Binary Type	Total Number	Original	Exchanged
BBH	8765	2248 (26 %)	6517 (74 %)
BH-NS	124	114 (92 %)	10 (8 %)
NS-NS	24	23 (96 %)	1 (4 %)
WD-WD	22992	21168 (92 %)	1824 (8 %)
WD-NS	786	750 (95 %)	36 (5 %)
WD-BH	395	157 (40 %)	238 (60 %)

For the purpose of this project, our focus lies on the BBHs and BH-NS systems. Although binary NSs also qualify as compact binaries, these were omitted due to the small sample size (Belczynski et al., 2018; Ye et al., 2020). For the BBHs and BH-NSs, the merger time t_{GW} was calculated according to equation (1.6). However, equation (1.6) uses the semi-major axis at the time of escape, $t_{\rm esc}$, meaning that $t_{\rm GW}$ is the time between the point of escape and the merging of the binary. Thus, in order to obtain the physical time at which the binary merges, we need to consider the delay time,

$$t_{\rm delay} = t_{\rm esc} + t_{\rm GW}. \tag{3.1}$$

Using equations (1.6) and (3.1), the delay time was calculated for all escaping BBHs and BH-NSs, and compared to the Hubble time, $t_H = 14$ Gyr. Binaries for which $t_{\rm delay} < t_H$ were labeled as *mergers*, and those for which $t_{\rm delay} > t_H$ as *nonmergers*. The total number of mergers, as well as the numbers of original and exchanged mergers, for BBHs and BH-NSs can be found in Table 3.2. It can be seen that the majority (72%) of the BBH mergers were exchanged ones, whereas the majority of the BH-NS (87%) were original ones. Dynamical exchange encounters occur during three-body encounters in which one of the binary components is replaced by an intruder. Exchange is most likely to occur if the mass of the intruder is larger than one of the binary components. Therefore, if a binary containing a BH and a low-mass component encounters a single BH, the single BH is likely to replace the low-mass component, resulting in the formation of a BBH. Therefore, a significant fraction of BBHs are formed in exchange encounters.

Table 3.2: Total number of BBHs and BH-NS that merge within a Hubble time, produced by the MOCCA-Survey Database II cluster models, along with the numbers (and percent) of original and exchanged mergers.

Binary Type	$N_{\rm merger}$	Original	Exchanged
BBH	3359	933 (28 %)	2426 (72 %)
BH-NS	61	53 (87 %)	8 (13 %)

3.2 Binary Black Holes

3.2.1 Escape Time and Delay Time

Fig. 3.1 shows the distribution of $t_{\rm esc}$ for the escaping BBHs. It can be seen that 89 % of the total number of original BBHs escape within the first Gyr. For nearly 50 % of these, we find that the escape occurred due to the kick received by the BBH center of mass following the formation of the second BH. Therefore, a significant fraction get ejected out very early on in cluster evolution. The remaining original binaries were ejected due to binary-single and binary-binary encounters with other BHs. For the exchanged BBHs, on the other hand, only 34% escape within the first Gyr, and the rest escape due to dynamical encounters at later times.

Fig. 3.2 shows the $t_{\rm delay}$ distribution for escaping BBHs. We see that $\sim$ 55% of the originally formed BBHs have $t_{\rm delay} < 1$ Gyr, meaning that they form, get ejected, and merge within 1 Gyr. The number of original BBHs that merge per Gyr then quickly decreases, and at 13 to 14 Gyr only about 1-2% of the escaping original BBHs merge. For the exchanged BBHs, only $\sim$ 35% have $t_{\rm delay} < 1$ Gyr, but the amount of mergers per Gyr does not decrease as quickly. Most of the merging original BBHs have lower semi-major axis values at escape time compared to exchanged binaries (See Section 3.2.3 and Fig. 3.9). This results in them having a shorter merger time due to gravitational wave radiation.

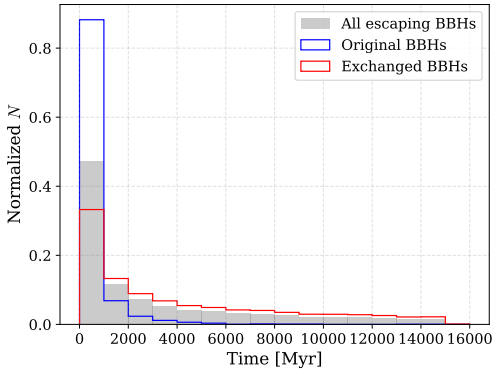

Figure 3.1: Time of escape in Myr for all escaping BBHs. The y-axis is normalized such that each bin is weighted by the total number of binaries falling into that bin, for all escaping BBHs (gray area), original (blue) BBHs and exchanged (red) BBHs, respectively.

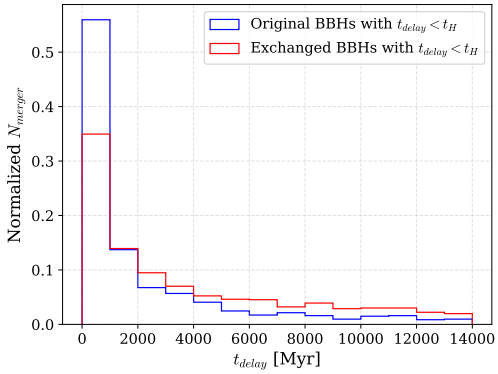

Figure 3.2: $t_{\rm delay}$ for the escaping BBHs that merge within a Hubble time. The y-axis is normalized such that each bin is weighted by the total number of binaries falling into that bin, for original (blue) and exchanged (red) BBHs, respectively.

3.2.2 Mass and LVK Comparison

Here, we seek to investigate parameters related to the mass of the escaping BBHs, and compare our findings with LVK detections. The LVK data used in this thesis was obtained from the LIGO Scientific Collaboration and Virgo Collaboration website for "Open data from the first and second observing runs of Advanced LIGO and Advanced Virgo"(Abbott et al., 2021).

First, we notice from Fig. 3.3, which shows the mass distribution for BBHs produced in the MOCCA models, that the total mass of the exchanged BBHs produced in the MOCCA models is shifted towards higher masses when comparing with original BBHs. This can be explained directly by the fact that the exchanged binaries are formed through binary-single encounters where the mass of the single intruder is greater than

the mass of either binary component. By replacing the lighter component, the intruder increases the mass of the binary.

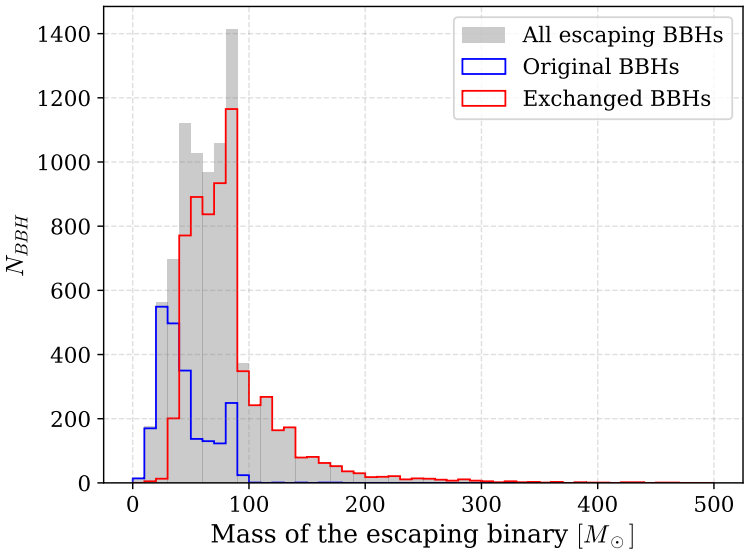

Figure 3.3: Total mass of escaping BBHs. Here, the gray area represents all escaping BBHs, and the blue and red lines represent original and exchanged ones, respectively.

Next, we consider only the BBHs with $t_{\rm delay} < t_H$ as these are comparable with the LVK data. Fig. 3.4 shows the normalized distribution of the total mass of escaping BBH mergers along with that of the LVK detections of BBHs. The normalization of the y-axis is such that each bin is weighted by the total number of entries falling into that bin, meaning that the values on the axis are fractions relative to the total numbers of BBHs in each of the categories (LVK detections, original BBHs with $t_{\rm delay} < t_H$, and exchanged BBHs with $t_{\rm delay} < t_H$).

Similar to what we saw in Fig. 3.3, BBHs with lower mass are more likely to have formed originally and evolved together, while those with higher mass are more likely to have formed in dynamical exchange encounters. The two distributions overlap in a region between roughly $30 - 100$ $M_\odot$. Furthermore, we see that the majority of the BBH mergers detected by LVK have masses in the range $10 - 120$ $M_\odot$, with a few ones having masses > 150 $M_\odot$. Based on the mass distributions for the simulated BBHs, one can say that LVK detections with total mass < 50 $M_\odot$ are more likely to have formed originally, whereas the ones with mass > 90 $M_\odot$ are more likely to have formed through dynamical interactions.

Similarly, the chirp masses (Cutler & Flanagan, 1994), defined as

$$\mathcal{M} = \frac{(m_1 m_2)^{3/5}}{(m_1 + m_2)^{1/5}}, \tag{3.2}$$

are centered around a higher value for the exchanged BBHs than the original ones, and the two regions overlap between approximately $10 - 40$ $M_\odot$, which can be seen in Fig. 3.5. Roughly 18% of the BBHs detected by LVH have chrip masses in the range $10 - 15$ $M_\odot$, and when comparing with the distributions from our simulated MOCCA models, we can see that these are likely to be original binaries. Furthermore, about 26% of the LVK detections have chirp masses in the range $35 - 40$ $M_\odot$. It is difficult to say whether these are formed originally or through exchange, but the probability of the latter is slightly higher based on the MOCCA distributions.

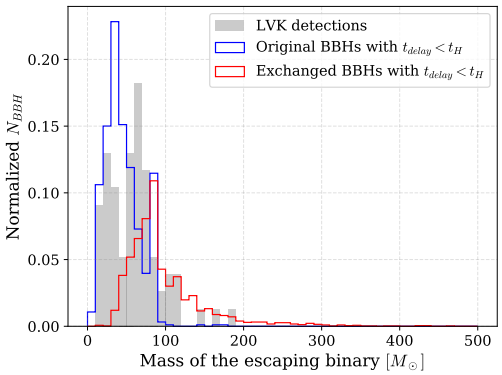

Figure 3.4: Normalized distribution of the total mass of the escaping BBHs for which $t_{\rm delay} < t_H$. Here, the blue line corresponds to original BBHs, the red line to exchanged ones, and the gray areas to LVK detections.

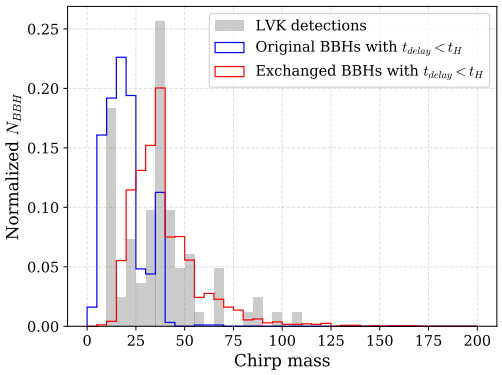

Figure 3.5: Normalized distribution of chirp masses for the escaping BBHs for which $t_{\rm delay} < t_H$. Here, the blue line corresponds to original BBHs, the red line to exchanged ones, and the gray areas to LVK detections.

Fig. 3.6 shows the mass ratio distribution for simulated BBHs with $t_{\rm delay} < t_H$ and $t_{\rm delay} > t_h$, respectively. Throughout this thesis, the mass ratio is defined as

$$q = \frac{m_2}{m_1}, \tag{3.3}$$

where m_1 is the mass of the heavier component, and m_2 that of the lighter one, meaning that we always have $0 < q \leq 1$. The two distributions follow a similar trend, and high mass ratios are clearly favoured, which agrees with the fact that merging BBHs are more likely to pair up equal mass BHs, regardless of their formation channel.

In Fig. 3.7, we present the mass ratio distribution for the produced BBH mergers. Here, it is important to note that the original BBHs are lower in number than the exchanged

ones (see Table 3.2), and the sample size might affect the distribution. From what can be seen in Fig. 3.7, it is difficult to determine the formation channel of an observed BBH based on mass ratio alone. However, we see that only a few percent of original BBHs have $q < 0.3$. Thus, observed BBHs with $q < 0.3$ are more likely to have formed through exchange encounters in GCs. These results are consistent with recent findings from direct N-body simulations of low-mass star clusters (Rastello et al., 2021; Trani et al., 2022).

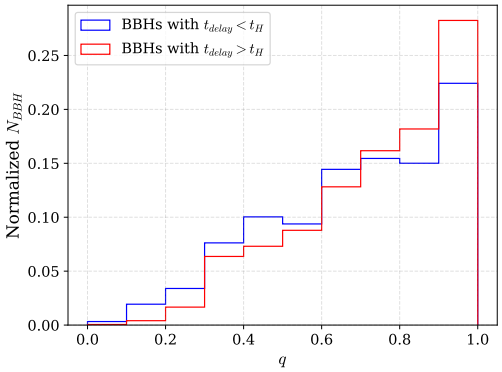

Figure 3.6: Normalized mass ratio distribution for BBHs with $t_{\rm delay} < t_H$ (blue) and $t_{\rm delay} > t_h$ (red), respectively.

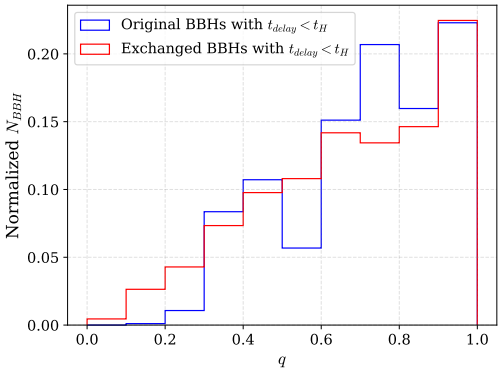

Figure 3.7: Normalized mass ratio distribution for original (blue) and exchanged (red) BBHs with $t_{\rm delay} < t_H$.

Fig. 3.8 shows m_2 plotted against m_1 for the MOCCA BBH mergers (original shown with blue points and exchanged shown with red points), along with the LVK detections (black points) and the corresponding error bars. From the MOCCA results, it can be seen that low-mass BBHs ($m_1, m_2 < 20$ M$_\odot$) are more likely to be original, whereas high-mass ones ($m_1, m_2 > 60$ M$_\odot$) are mostly likely to have formed through exchange encounters. This includes LVK detected events like GW190521, GW200220 and GW190426.

Furthermore, we see an overdensity in points along a horizontal axis at $m_2 \approx 45$M$_\odot$ and 45 M$_\odot$ $< m_1 <$ 90 M$_\odot$. 45 M$_\odot$ is the maximum mass of a BH produced in our simulations through stellar evolution. The over-density in points indicates second generation BHs (that formed from the merger of 2 first generation BHs inside the cluster) merging with a first generation BH. If the two first generation 45 M$_\odot$ BHs merge to form a second generation BH of around 90 M$_\odot$ then this BH is likely to pair up with another first generation BH in three-body encounter.

We can also relate Fig. 3.8 to the mass ratio seen in Fig. 3.7, where we concluded that BBHs with $q < 0.3$ are more likely to be formed through exchange. The lower right parts of Fig. 3.8 clearly show that the majority of simulated BBHs with low mass ratios,

or $m_1 > 60$ M$_\odot$ and $m_2 < 40$ M$_\odot$ are dynamically formed in exchange encounters. Two such LVK detections (GW190403 and GW190929) with masses $m_1 \approx 80 - 90$ M$_\odot$ and $m_2 \approx 20 - 25$ M$_\odot$ can be identified.

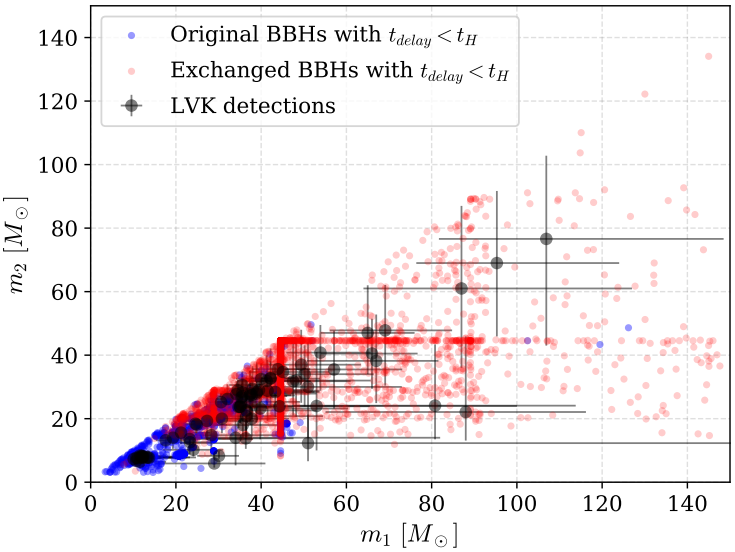

Figure 3.8: Mass m_2 of the lighter component plotted against mass m_1 of the heavier component for original (blue) and exchanged (red) BBHs with $t_{\rm GW} < t_H$. The corresponding values for mergers detected by LVK (black) are plotted on top along with their respective error bars.

3.2.3 Semi-major Axis and Eccentricity

In Figs. 3.9 and 3.10, we see the distribution of the semi-major axis and eccentricity, respectively, of all escaping BBHs. We see that BBHs that do not merge within a Hubble time are shifted towards larger semi-major axes values compared to the ones that merge. This can be explained as a smaller semi-major axis implies a harder binary, and harder binaries merge quicker than soft ones (Peters, 1964; Rodriguez et al., 2015). Furthermore, original binaries have lower semi-major axis compared to exchanged ones. This is due to the fact that the components in original BBHs go through stellar evolution together as a bound system, which circularizes the orbit and shrinks the semi-major axis (Hurley et al., 2002; Mapelli, 2020). Thus, we expect original BBHs to have a more uniform eccentricity distribution, which can be seen in Fig. 3.10, regardless of whether the binary merges within a Hubble time or not. Conversely, exchanged binaries are shifted towards higher eccentricity values. Dynamical encounters can increase the eccentricity of these systems.

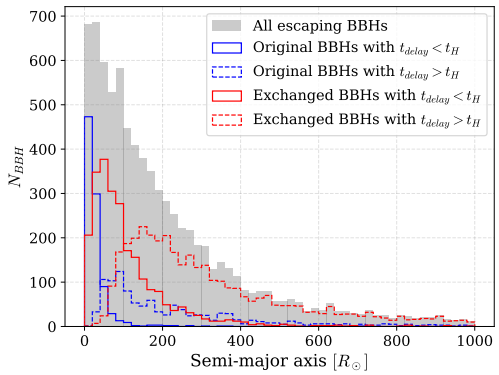

Figure 3.9: Semi-major axis distribution for all escaping BBHs (gray), original BBHs (blue) with $t_{\rm delay} < t_H$ (solid line) and $t_{\rm delay} > t_H$ (dashed line), and exchanged BBHs (red) with $t_{\rm delay} < t_H$ (solid line) and $t_{\rm delay} > t_H$ (dashed line), respectively.

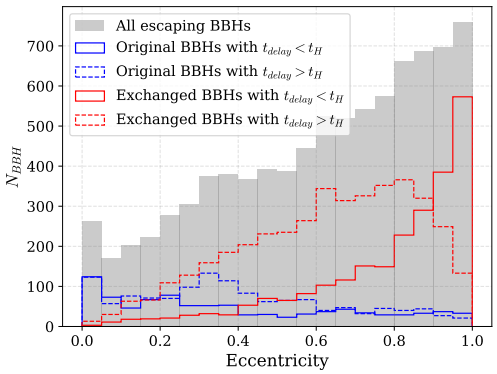

Figure 3.10: Eccentricity distribution for all escaping BBHs (gray), original BBHs (blue) with $t_{\rm delay} < t_H$ (solid line) and $t_{\rm delay} > t_H$ (dashed line), and exchanged BBHs (red) with $t_{\rm delay} < t_H$ (solid line) and $t_{\rm delay} > t_H$ (dashed line), respectively.

3.3 BH-NS Systems

3.3.1 Escape Time and Delay Time

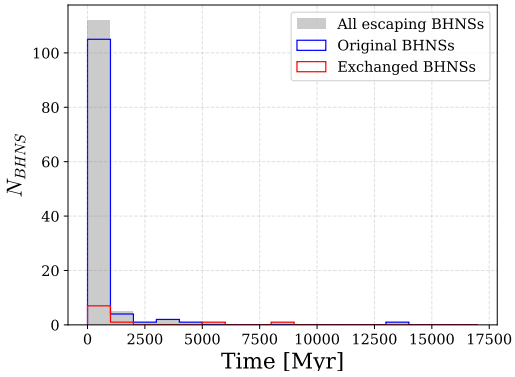

Figure 3.11: Time of escape in Myr for all escaping BH-NS binaries. The gray area represents all escaping BH-NS while the blue and red lines show the original and exchanged BH-NSs, respectively.

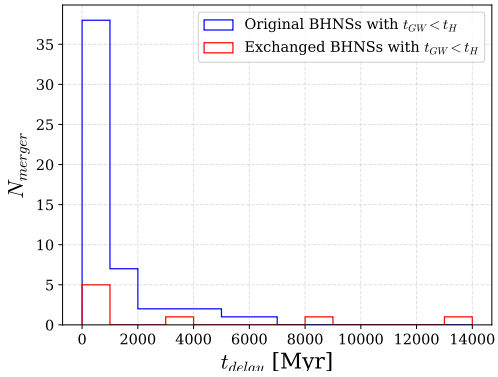

Figure 3.12: $t_{\rm delay}$ for the escaping BH-NSs that merge within a Hubble time. The y-axis is normalized such that each bin is weighted by the total number of binaries falling into that bin.

Figures 3.11 and 3.12 show the distributions of $t_{\rm esc}$ and $t_{\rm delay}$ for the escaping BH-NS systems. Due to the small population of exchanged BH-NSs, it is difficult to conclude anything regarding these. However, for the original binaries, the majority (92%) are found to escape within the first Gyr, which is similar to what we saw for BBHs. Furthermore, about 37% of the escaping BH-NS systems merge within one Gyr, and only a few percent merge after 2 Gyr.

3.3.2 Mass and LVK Comparison

Fig. 3.13 shows the total mass distribution of the escaping BH-NS systems. Despite the small sample size of exchanged BH-NSs, original BH-NS appears to be shifted towards lower masses compared to the exchanged ones, which is in agreement with the BBH findings.

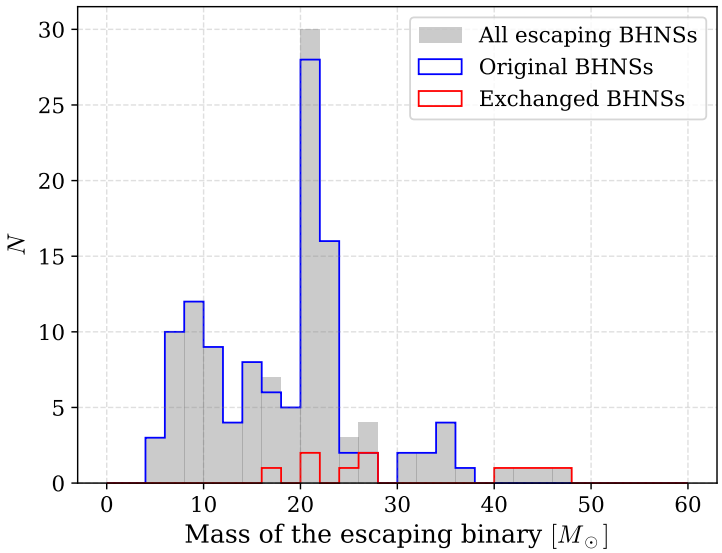

Figure 3.13: Total mass of escaping BH-NS binaries. Here, the gray area represents all escaping BH-NSs, the blue line original BH-NSs, and the red line exchanged BH-NSs.

Next, we investigate the mass ratio distribution of BH-NS systems, which is presented in Figs. 3.14 and 3.15. From Figs. 3.15 and 3.16, it becomes clear that mass ratios lower than 0.2 are especially favourable for exchanged binaries that do merge within a Hubble time. In Fig. 3.16, we see that binaries where the BH mass $m_1 < 20$ M$_\odot$ are more likely to be formed originally, whereas those with $m_1 > 20$ M$_\odot$ are more likely to be formed through interactions. Based on this, we can identify three LVK detections with $m_1 < 10$ M$_\odot$ that are most likely original binaries, and three with $m_1 > 10$ M$_\odot$ that are most likely exchanged ones.

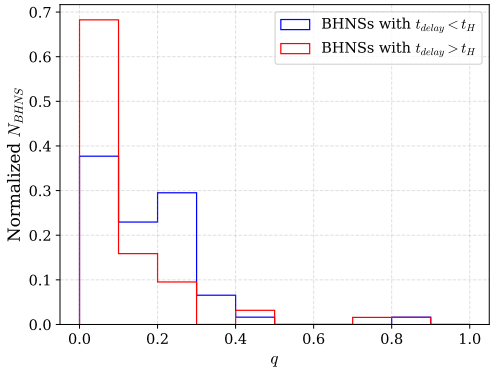

Figure 3.14: Normalized mass ratio distribution for BH-NSs with $t_{\text{delay}} < t_H$ (blue) and $t_{\text{delay}} > t_h$ (red), respectively.

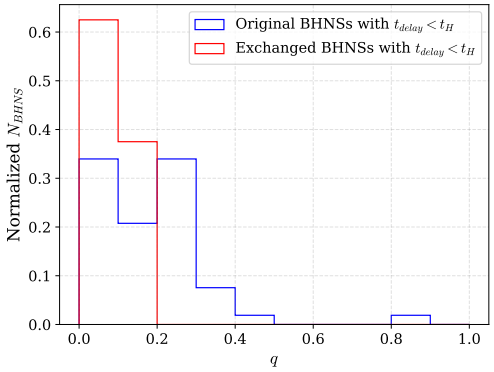

Figure 3.15: Normalized mass ratio distribution for original (blue) and exchanged (red) BH-NSs with $t_{\text{delay}} < t_H$.

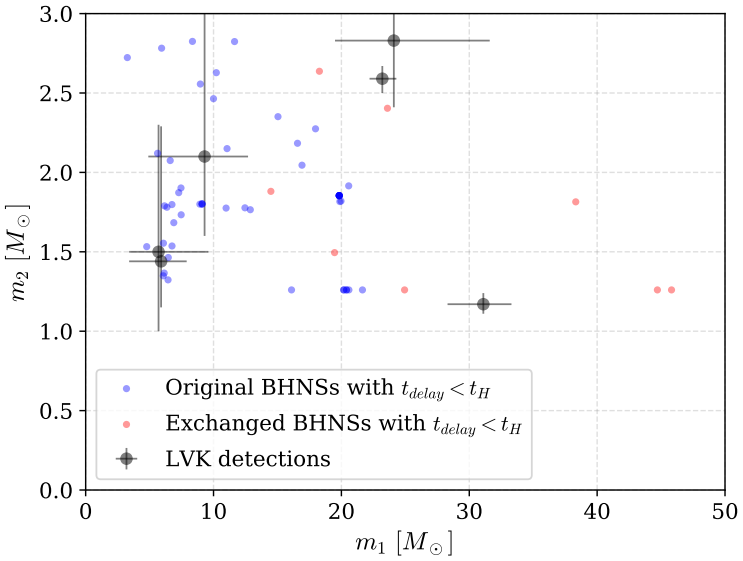

Figure 3.16: Mass m_2 of the lighter component plotted against mass m_1 of the heavier component for original (blue) and exchanged (red) BH-NSs with $t_{\text{GW}} < t_H$. The corresponding values for mergers detected by LIGO (black) are plotted on top along with their respective error bars.

3.4 Global Cluster Properties

The aim with the results presented in this section is to investigate and reproduce correlations between the number of merging binaries produced in a cluster and the initial parameters of that particular cluster model that were found by Hong et al. (2018). They found a strong logarithmic relation between the number of produced merging BBHs and a parameter, γ, which they defined as

$$\gamma = A \cdot \frac{M_0}{10^5 \mathrm{M}_\odot} \cdot \left(\frac{\rho_h}{10^5 \mathrm{M}_\odot \mathrm{pc}^{-3}} \right)^\alpha + B \cdot \frac{M_0}{10^5 \mathrm{M}_\odot} \cdot f_{b,0}, \tag{3.4}$$

where M_0, ρ_h and $f_{b,0}$ are the initial total mass, half-mass density and initial primordial binary fraction, and $A,\ B,\ \alpha$ are fitting parameters, $(A, B, \alpha) = (12.53 \pm 0.22, 6.89 \pm 0.84, 0.33 \pm 0.02)$ (Hong et al., 2018). When attempting to plot this on all the merging BBHs from our simulated models, we did not see a clear correlation between γ and the number of merging BBHs. Hence, we chose to focus on a smaller group of models with similar initial conditions, specifically those where the two simulated populations have initial upper mass limits `mup`= 150.0, 150.0. This was further separated into two subsets with initial tidal radii $r_{\mathrm{t},0} = 60$ pc, and $r_{\mathrm{t},0} = 120$ pc, respectively. For each of these subsets, the fraction of produced BBHs that merge within a Hubble time relative to the total number of produced BBHs, $N_{\mathrm{merger}}/N_{\mathrm{BBH}}$, was plotted against the initial central cluster density, which can be seen in Figs. 3.17 and 3.18 for $r_{\mathrm{t},0} = 60$ pc, and $r_{\mathrm{t},0} = 120$ pc, respectively.

The relation between $N_{merger}/N_{\mathrm{BBH}}$ and initial central cluster density $\rho_{c,0}$ was fitted in `Python` using the tool `polyfit` from the `numpy` library, which resulted in relations on the form

$$\frac{N_{merger}}{N_{BBH}} = \rho_{c,0}^k \cdot 10^m \tag{3.5}$$

where k and m are fitting parameters. For the models with $r_{t,0} = 60$ pc in Fig. 3.17, we find $(k_{60}, m_{60}) = (0.1478 \pm 0.0298, -1.325 \pm 0.185)$, and for those with $r_{t,0} = 120$ pc in Fig. 3.18, we find $(k_{120}, m_{120}) = (0.1099 \pm 0.0511, -1.061 \pm 0.330)$. Thus, the correlation is stronger for the models with $r_t = 60$ pc compared to those with $r_t = 120$ pc, in the sense that the errors are smaller for the former fit than the latter. Here, it should be noted that the sample size for $r_t = 60$ pc is greater than that for $r_t = 120$ pc.

Furthermore, we have highlighted the models that host an IMBH at 12 Gyr in order to compare our results with Hong et al. (2020), who found that GC models that form an IMBH early on their evolution have significantly reduced production of merging BBHs. The presence of a central IMBH can eject out BHs preventing them to form binary systems in exchange encounters (Leigh et al., 2014). Similar to Hong et al. (2020), we find a tendency that models containing more massive IMBHs have a reduced number of merging BBHs. In some cases, they also produce a lower fraction of merging BBHs

as indicated by the green points in Figs 3.19 and 3.20. The x-axis in these figures is defined as

$$\delta = \frac{M_0}{10^5 \mathrm{M}_\odot} \cdot \left(\frac{\rho_h}{10^6 \mathrm{M}_\odot \mathrm{pc}^{-3}} \right)^{0.33}, \tag{3.6}$$

where the parameter δ is a slightly modified version of a parameter (given by the first term in equation (3.4)) used by Hong et al. (2020). For the data shown in Figs. 3.19 and 3.20, the relations between the merger fractions and δ were fitted. The resulting relations are on the form

$$\frac{N_{merger}}{N_{BBH}} = \delta^a \cdot 10^b, \tag{3.7}$$

where we find $(a_{60}, b_{60}) = (0.3799 \pm 0.0848, -0.7916 \pm 0.0878)$, and $(a_{120}, b_{120}) = (0.1876 \pm 0.1372, -0.5572 \pm 0.1525)$. Once again, we find that the correlation is stronger for the denser model. However, the sample size is also larger for the $r_t = 60$ pc models than for the $r_t = 120$ pc models.

The Hong et al. (2018) paper made use of a limited set of MOCCA models (with low initial binary fraction) that were simulated with an old version of the MOCCA code, while the Hong et al. (2020) paper made use of MOCCA-Survey Database I simulations. In this project, however, we used data from MOCCA-Survey Database II, which contains several updates compared to earlier versions (see Chapter 2). These models have not been analyzed before for the purpose of studying merging stellar-mass binary BHs or BH-NS binaries. Thus, we expect some differences between our results and those from Hong et al. (2018) and Hong et al. (2020). This could explain why we see a wider spread in our points compared to what was seen in the Hong et al. (2018) and Hong et al. (2020) papers. However, what can be said based on our results is that clusters with higher initial central density and total mass tend to produce a higher fraction of merging BBHs, which is in agreement with the results from Hong et al. (2018).

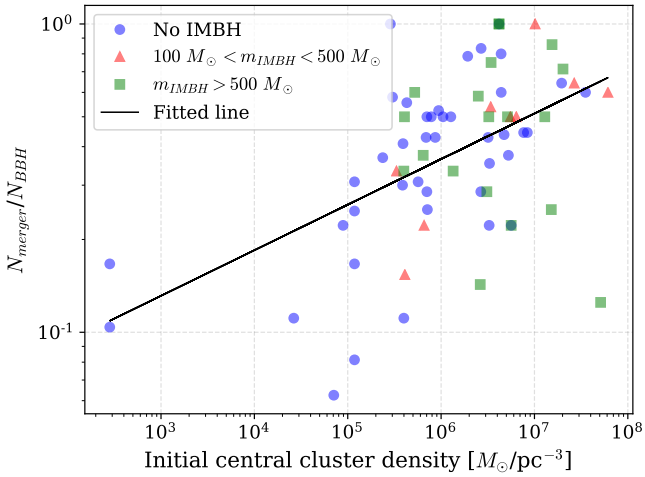

Figure 3.17: The fraction of BBH mergers produced in each model plotted against the initial central cluster density $\rho_{c,0}$ for clusters with $r_{t,0} = 60$ pc. Blue points correspond to clusters that do not form an IMBH within 12 Gyr, red triangles corresponds to clusters with an IMBH with mass 100 $M_\odot$ < $m_{\rm IMBH}$ < 500$M_\odot$, and green squares correspond to cluters that form an IMBH with mass $m_{\rm IMBH} > 500 M_\odot$. The fitted line has equation $N_{merger}/N_{\rm BBH} = \rho_{c,0}^{0.1478} \cdot 10^{-0.0298}$.

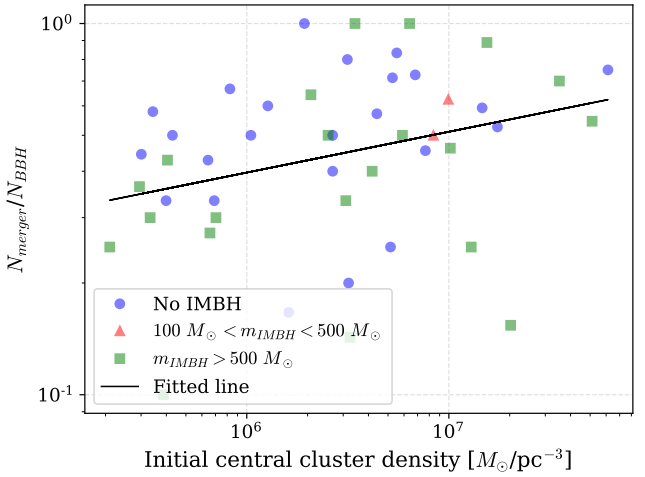

Figure 3.18: The fraction of BBH mergers produced in each model plotted against the initial central cluster density $\rho_{c,0}$ for clusters with $r_{t,0} = 120$ pc. Blue points correspond to clusters that do not form an IMBH within 12 Gyr, red triangles corresponds to clusters with an IMBH with mass 100 $M_\odot$ < $m_{\rm IMBH}$ < 500$M_\odot$, and green squares correspond to cluters that form an IMBH with mass $m_{\rm IMBH} > 500 M_\odot$. The fitted line has equation $N_{merger}/N_{\rm BBH} = \rho_{c,0}^{0.1099} \cdot 10^{-1.061}$.

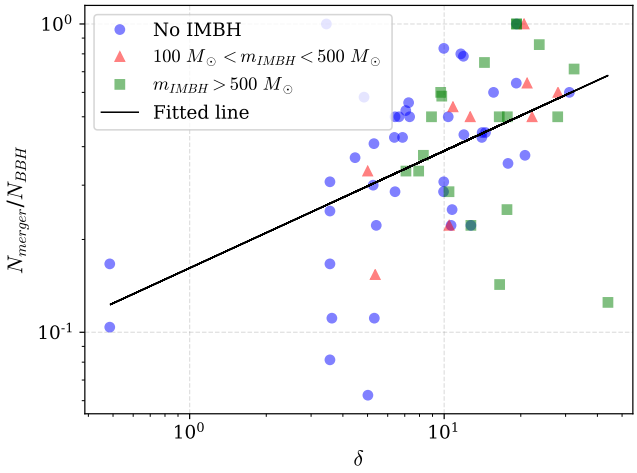

Figure 3.19: The fraction of BBH mergers produced in each model plotted against δ for clusters with $r_{t,0} = 60$ pc. Blue points correspond to clusters that do not form an IMBH within 12 Gyr, red triangles corresponds to clusters with an IMBH with mass 100 $M_\odot < m_{\rm IMBH} < 500 M_\odot$, and green squares correspond to cluters that form an IMBH with mass $m_{\rm IMBH} > 500 M_\odot$. The fitted line has equation $N_{merger}/N_{\rm BBH} = \rho_{c,0}^{0.3799} \cdot 10^{-0.7916}$.

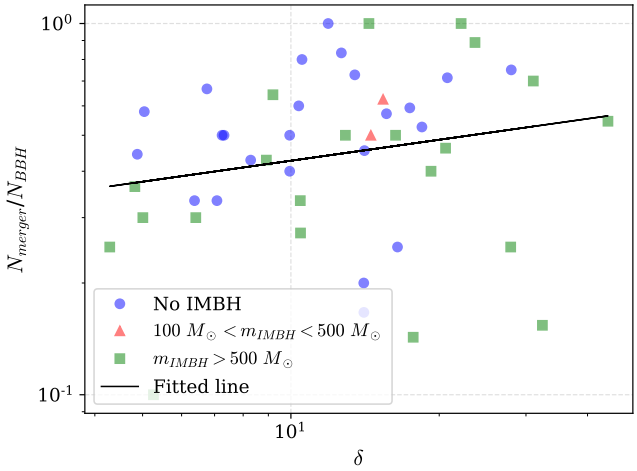

Figure 3.20: The fraction of BBH mergers produced in each model plotted against δ for clusters with $r_{t,0} = 120$ pc. Blue points correspond to clusters that do not form an IMBH within 12 Gyr, red triangles corresponds to clusters with an IMBH with mass 100 $M_\odot < m_{\rm IMBH} < 500 M_\odot$, and green squares correspond to cluters that form an IMBH with mass $m_{\rm IMBH} > 500 M_\odot$. The fitted line has equation $N_{merger}/N_{\rm BBH} = \rho_{c,0}^{0.1876} \cdot 10^{-0.5572}$.

3.4.1 IMBHs and BH Retention

In this section, we present a closer investigation of the relation between the initial cluster properties, BH retention, and subsequent development of the cluster. First, we examine five different cluster models, all of which have $N = 400000,\ 400000$, $W_0 = 6.0,\ 6.0$, mup $= 150.0,\ 150.0$, $r_t = 60.0$, conc_pop $= 0.1$ and a binary fraction of $f_b = 0.1$. The difference between these five clusters is their initial half-mass radius, which is presented in Table 3.3 along with specific properties taken at the 12 Gyr timestamp for each of the models. Furthermore, the model with initial half-mass radius $r_{\mathrm{hm},0} = 0.6$ pc hosts a central IMBH, while the other models have central BHSs instead.

Similarly, we compare two other cluster models with similar initial properties except for the initial half-mass radius. The initial parameters are $N = 400000,\ 200000$, $W_0 = 6.0,\ 6.0$, mup $= 150.0,\ 150.0$, $r_t = 60.0$, conc_pop $= 0.5$ and $f_b = 0.95$, and specific properties taken at the 12 Gyr timestamp for each of the models can be found in Table 3.4. The model with initial half-mass radius $r_{\mathrm{hm},0} = 0.6$ pc hosts a central IMBH, while the one with $r_{\mathrm{hm},0} = 1.2$ pc has a central BHS instead.

Table 3.3: Properties for five different cluster models. The properties presented in this table are the initial half-mass radius $r_{\mathrm{hm},0}$, as well as the number of single BHs N_{BBH}, BBHs N_{BBH}, maximum BH mass $M_{\mathrm{BH,\ max}}$ and half-mass radius $r_{\mathrm{hm},12}$ taken at the 12 Gyr timestamp.

$r_{\mathrm{hm},0}$ [pc]	N_{BH}	N_{BBH}	$M_{\mathrm{BH,\ max}}$ $[M_\odot]$	$r_{\mathrm{hm},12}$ [pc]	IMBH
0.6	4	0	$1.89 \cdot 10^4$	4.32	Yes
1.2	365	2	32.6	6.68	No
2.0	443	7	45.6	7.56	No
4.0	412	4	45.5	7.96	No
6.0	365	6	45.5	8.18	No

Table 3.4: Properties for two cluster models. The properties presented in this table are the initial half-mass radius $r_{\mathrm{hm},0}$, as well as the number of single BHs N_{BH}, BBHs N_{BBH}, maximum BH mass $M_{\mathrm{BH,\ max}}$ and half-mass radius $r_{\mathrm{hm},12}$ taken at the 12 Gyr timestamp.

$r_{\mathrm{hm},0}$ [pc]	N_{BH}	N_{BBH}	$M_{\mathrm{BH,\ max}}$ $[M_\odot]$	$r_{\mathrm{hm},12}$ [pc]	IMBH
0.6	24	0	692	2.90	Yes
1.2	498	5	40.2	4.99	No

Cluster Evolution and BH Retention

In Figs 3.21 and 3.22, we see three panels illustrating the cluster evolution for the models presented in Tables 3.3 for $f_b = 0.1$ and 3.4 for $f_b = 0.95$, respectively. Both binary fractions show similar trends. We see that the BH retention is significantly lower for clusters with a central IMBH compared to those with a BHS. BHs evaporate very quickly, especially within the first 2.5 Gyr for models with an IMBH, and the number of retained BHs approach zero at around 10 Gyr in those models. On the other hand, models with a BHS can retain more than 500 BHs at 10 Gyr. Furthermore, $r_{\rm hm}$ increases at a slower rate for models with an IMBH than for those without one. The total cluster mass initially decreases quickly for all models, but the rate at which this happens becomes lower for IMBH models than BHS models after about 5 Gyr.

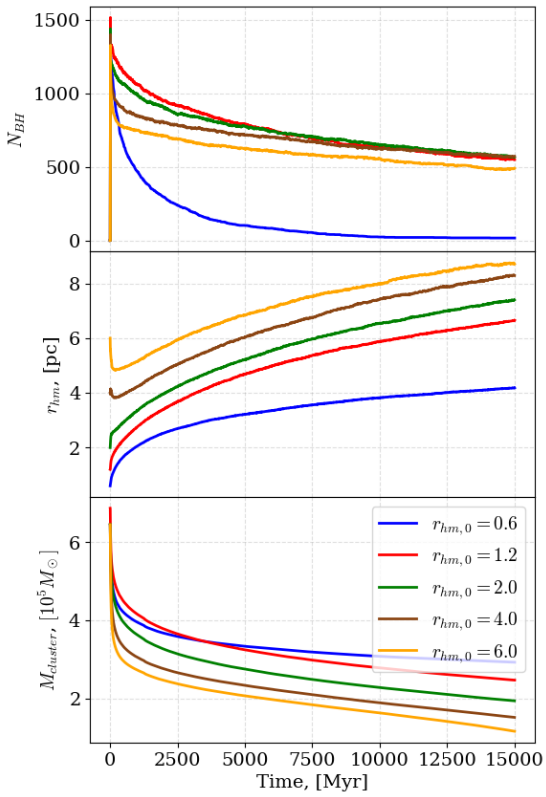

Figure 3.21: Cluster evolution comparison for the models presented in Table 3.3. The top panel shows the BH retention over time, the middle panel shows how the half-mass radius changes over time, and the bottom panel shows how the total cluster mass changes over time.

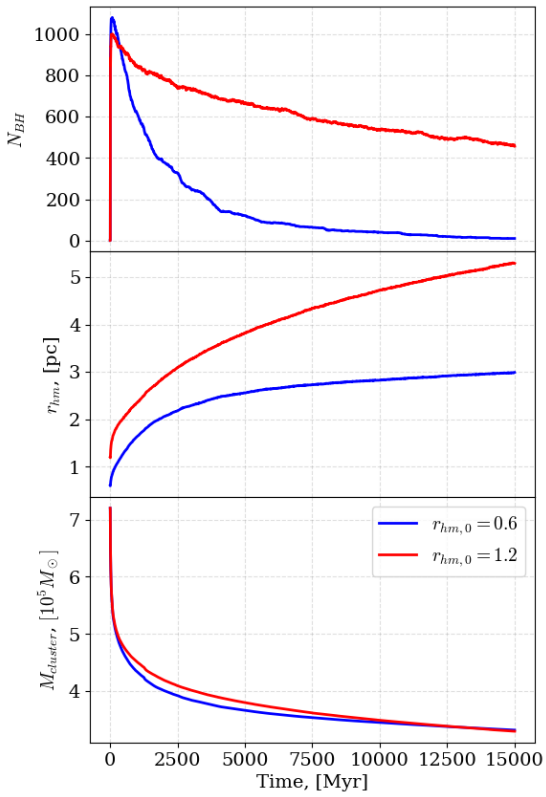

Figure 3.22: Cluster evolution comparison for the models presented in Table 3.4. The top panel shows the BH retention over time, the middle panel shows how the half-mass radius changes over time, and the bottom panel shows how the total cluster mass changes over time.

In Fig 3.23, we see the number of BBHs formed in the $f_b = 0.1$ models with $r_{\rm hm,0} = 1.2$ pc and $r_{\rm hm,0} = 4.0$ pc. The numbers fluctuate rapidly due to the formation and ejection of BBHs as the cluster evolves. Hence, we consider the moving average, which shows that the number of BBHs is on average higher at all times for the denser model with $r_{\rm hm,0} = 1.2$ than for the less dense model with $r_{\rm hm,0} = 4.0$ pc.

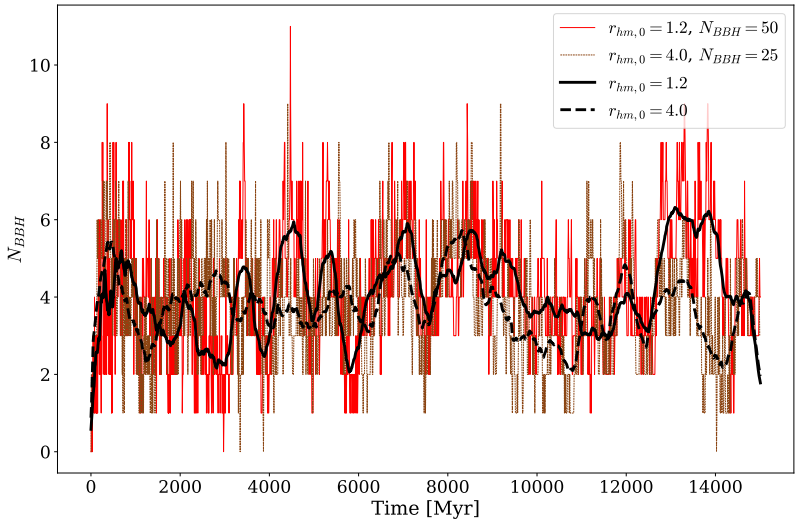

Figure 3.23: The number of BBHs formed in the simulated cluster models with initial half-mass radius ($r_{\rm hm,0}$) of 1.2 pc (red line) and 4.0 pc (brown line). The variation in the number indicates that BBHs are forming and being ejected or dissolved throughout the cluster evolution. The black solid line shows the moving average for the number of BBHs in the $r_{\rm hm,0}$=1.2 pc model and the dashed black line shows it for $r_{\rm hm,0}$=4.0 model. The model with $r_{\rm hm,0}$ =1.2 pc produces twice as many escaping BBHs compared to the model with $r_{\rm hm,0}$=4.0 pc.

Relation Between Semi-major Axis of BBHs and Initial Cluster Density

In order the distribution of semi-major axis of the BBHs that escape from the models described in Table 3.3 and 3.4, we have plotted the cumulative distributions of the semi-major axes for escaping BBHs escaping from each model. This can be seen in Figs 3.24 and 3.25 for $f_b = 0.1$ and $f_b = 0.95$, respectively. We see that the semi-major axis is shifted towards larger values for models with lower initial density and larger initial half-mass radius. In Section 3.2.3, we saw that binaries that merge within a Hubble time tend to have lower semi-major axes than those that do not merge. Hence, cluster models with high initial densities are more likely to form merging BBHs. This also explains the increasing trend in the fraction of merging BBHs vs density plot shown in Fig. 3.19.

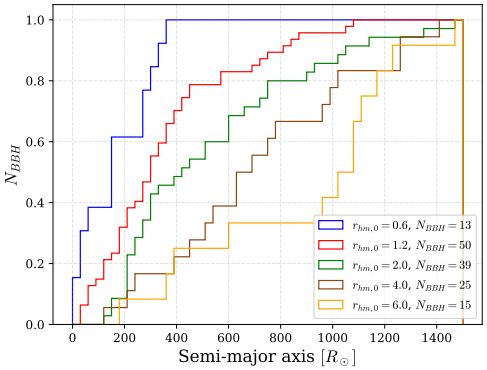

Figure 3.24: Cumulative histogram of the semi-major axis of the escaping BBHs produced in the models presented in Table 3.3. The y-axis is normalized such that the total counts equals unity.

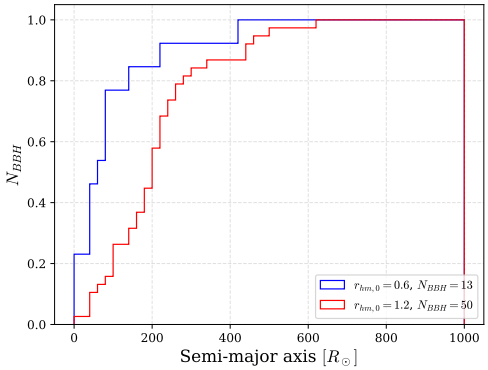

Figure 3.25: Cumulative histogram of the semi-major axis of the escaping BBHs produced in the models presented in Table 3.4. The y-axis is normalized such that the total counts equals unity.

In Fig. 3.26, we see the distribution of velocities at which the BBHs escape, for BBHs produced in all the simulated cluster models. Thus, these velocities must be greater than the escape velocities (see equation (1.4)) of the respective cluster models. BBHs that will merge within a Hubble time are shifted towards higher escape velocities compared to those that do not merge. This indicates that they originate from denser models that have higher potentials, and thus higher escape velocities. These binaries can harden significantly before being ejected from the cluster (as seen in Figs 3.24 and 3.25). Furthermore, original BBHs that merge within the age of the Universe tend to have slightly higher escape velocities than those formed through dynamical interactions. This can be due to the kicks which these binaries can receive when the second binary component evolves into a BH. As stated in Section 3.2.1, nearly 50% of the original BBHs are ejected due to the kick the binary center of mass receives following the formation of the second BH.

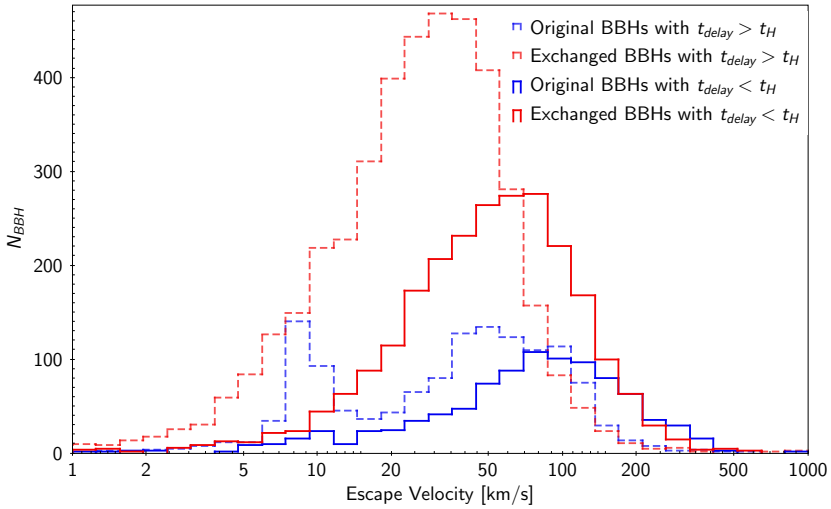

Figure 3.26: Distribution of velocities at which the BBHs escape from their cluster. Similar to Fig. 3.9, the original BBHs that merge within the age of the Universe are indicated in solid blue while the ones that do not merge are shown with dashed blue. The exchanged BBHs that merge within the age of the Universe are shown in red and the non-merging ones are shown in dashed red.

Chapter 4

Conclusions

We analyzed results from 281 simulated GC models to investigate the number and properties of escaping BBHs and BH-NS binaries. Using the properties at the time of escape, we estimated the time it would take these binaries to merge due to gravitational wave radiation. Focusing on BBHs, we find that

- A total of 8765 BBHs escape from all the models that were analysed. Out of these, 74% were formed due to dynamical exchange encounters and the remaining 26% formed from the evolution of two massive stars that were initially in a binary system (original binaries). 38% of all escaping BBHs merge due to gravitational wave radiation within a Hubble Time. About 72% of these formed through exchange encounters and the remaining 28% were original binaries.

- Nearly 90% of original BBHs have delay time values which are less than 1 Gyr. This means that original BBHs end up merging due to gravitational wave radiation shortly after their birth. The exchanged BBHs have a wider distribution in delay times and can take up to few to ten Gyrs to merge. These differences are reflected in the properties of the escaping BBHs. Merging exchanged BBHs have semi-major axis values that go up to 400 $R_\odot$ and they also have eccentricity values that increase towards 1. On the other hand, most of the merging original binaries have semi-major axis values less than about a 100 $R_\odot$ and they a more uniform eccentricity distribution.

- We find that some exchanged BBHs can have large component masses ($M \gtrsim$ 50 $M_\odot$). Observed LVK merging BBHs like GW190426, GW190521, GW200220 are more likely to have formed from dynamical exchange encounters rather than original binaries.

- We also find that a fraction of exchanged BBHs can have mass ratios less than 0.3. None of the original BBHs from our simulated models have such low-mass ratio values. Therefore, observed LVK BBHs where the mass ratio of the merging BHs is less than 0.3, such as GW190403 and GW190929, are consistent with dynamical formation in a GC. However, we must be cautious since there are significant error

bars on the observed component masses of LVK events. If more such events with better mass constraints are detected then they maybe indicative of formation in dense stellar clusters.

Focusing on BH-NS binaries, we find that

- We find a total of 124 escaping BH-NS binaries from all the stellar cluster models. About 92% of these are original binaries and only 8% form in dynamical exchange encounters.
- Only 61 BH-NS binaries that we identified will merge due to gravitational wave radiation within the age of the Universe. Most of these have semi-major axis values less than 10 $R_\odot$. Due to low number of these binaries it is difficult to see clear differences between the binary properties at escape times between original and exchanged binaries.
- Dynamical exchanges can form BH-NS systems where the BH mass is more than 20 to 30 $M_\odot$. While the majority of original BH-NS systems have BH masses less than 15 $M_\odot$. This also causes an increase in low-mass ratio ($q \lesssim 0.1$) mergers from exchanged BH-NS binaries. Based on these findings, we suggest that the LVK observed events GW191219 and GW190814 may have had dynamical origins. On the other hand, events like GW190426_152155 and GW200115 are consistent with merging original BH-NS systems that we find in our simulations.

Concerning the initial properties of GCs that produce merging BBHs, we typically find that initially dense clusters produce a higher fraction of merging BBHs. However, we find that extremely dense clusters ($\rho_0 \gtrsim 10^7$ $M_\odot$ pc^{-3}) that form an IMBH decrease the number of escaping merging BBHs. This is consistent with the recent work from Hong et al. (2020). We found that the semi-major axis value at the time of escape strongly correlates with the initial density and half-mass radius of the host cluster. Clusters with higher density and smaller initial half-mass radius produce escaping binaries with smaller semi-major axis values. Therefore, a higher fraction of BBHs escaping from these models are likely to merge within a Hubble time. Consequently, the escape velocity of BBHs that merge within a Hubble time are systematically higher than for those that do not merge within a Hubble time.

Future observations by LVK will result in a large number of detected gravitational wave events which can then be statistically compared with properties predicted from different formation channels. Dynamical exchanges predict the presence of BBH events in which component masses can be in the IMBH mass range. Seeing such events would be a strong indicator for dynamical formation. Additionally, better limits and error bars on observed compact object masses and spin distributions will be helpful in constraining their formation channel.

Bibliography

Abbott, R., Abbott, T. D., Abraham, S., et al. 2020, PRL, 125, 101102

Abbott, R., Abbott, T. D., Abraham, S., et al. 2021, SoftwareX, 13, 100658

Askar, A., Davies, M. B., & Church, R. P. 2021, MNRAS, 502, 2682

Askar, A., Szkudlarek, M., Gondek-Rosińska, D., Giersz, M., & Bulik, T. 2017, MNRAS, 464, L36

Belczynski, K., Askar, A., Arca-Sedda, M., et al. 2018, A&A, 615, A91

Benacquista, M. J. & Downing, J. M. B. 2013, Living Reviews in Relativity, 16, 4

Binney, J. & Tremaine, S. 2008, Galactic Dynamics: Second Edition

Chandrasekhar, S. 1942, Principles of stellar dynamics

Cohn, H. & Hut, P. 1984, ApJL, 277, L45

Cutler, C. & Flanagan, É. E. 1994, , 49, 2658

Davies, M. B. 2013, in Planets, Stars and Stellar Systems. Volume 5: Galactic Structure and Stellar Populations, ed. T. D. Oswalt & G. Gilmore, Vol. 5, 879

Di Carlo, U. N., Giacobbo, N., Mapelli, M., et al. 2019, MNRAS, 487, 2947

Fregeau, J. M., Cheung, P., Portegies Zwart, S. F., & Rasio, F. A. 2004, MNRAS, 352, 1

Fukushige, T. & Heggie, D. C. 2000, MNRAS, 318, 753

Giersz, M. 2006, MNRAS, 371, 484

Giersz, M., Heggie, D. C., Hurley, J. R., & Hypki, A. 2013, MNRAS, 431, 2184

Giersz, M., Leigh, N., Hypki, A., Lützgendorf, N., & Askar, A. 2015, MNRAS, 454, 3150

Harris, W. E., Harris, G. L. H., & Alessi, M. 2013, ApJ, 772, 82

Heggie, D. & Hut, P. 2003, The Gravitational Million-Body Problem: A Multidisciplinary Approach to Star Cluster Dynamics

Heggie, D. C. 1975, MNRAS, 173, 729

Hénon, M. 2011, arXiv e-prints, arXiv:1103.3499

Hénon, M. H. 1971, ApSS, 14, 151

Hills, J. G. 1975, AJ, 80, 809

Hong, J., Askar, A., Giersz, M., Hypki, A., & Yoon, S.-J. 2020, MNRAS, 498, 4287

Hong, J., Vesperini, E., Askar, A., et al. 2018, MNRAS, 480, 5645

Hurley, J. R., Pols, O. R., & Tout, C. A. 2000, MNRAS, 315, 543

Hurley, J. R., Tout, C. A., & Pols, O. R. 2002, MNRAS, 329, 897

Hypki, A. & Giersz, M. 2013, MNRAS, 429, 1221

Hypki, A., Giersz, M., Hong, J., et al. 2022, arXiv e-prints, arXiv:2205.05397

Kamlah, A. W. H., Leveque, A., Spurzem, R., et al. 2022, MNRAS, 511, 4060

Karttunen, H., Kröger, P., Oja, H., Poutanen, M., & Donner, K. J. 2017, Fundamental Astronomy

King, I. R. 1966, AJ, 71, 64

Kroupa, P. 2001, MNRAS, 322, 231

Küpper, A. H. W., Maschberger, T., Kroupa, P., & Baumgardt, H. 2011, MNRAS, 417, 2300

Leigh, N. W. C., Lützgendorf, N., Geller, A. M., et al. 2014, MNRAS, 444, 29

Madrid, J. P., Leigh, N. W. C., Hurley, J. R., & Giersz, M. 2017, MNRAS, 470, 1729

Maliszewski, K., Giersz, M., Gondek-Rosińska, D., Askar, A., & Hypki, A. 2021, arXiv e-prints, arXiv:2111.09223

Mapelli, M. 2017a, Binaries and 3-Body Encounters, url: `http://web.pd.astro.it/mapelli/2017dynamics3.pdf`

Mapelli, M. 2017b, Core Collapse and Reversal, url: `http://web.pd.astro.it/mapelli/2017dynamics2.pdf`

Mapelli, M. 2017c, Star Clusters as Collisional Systems, url: `http://web.pd.astro.it/mapelli/2017dynamics1.pdf`

Mapelli, M. 2020, Frontiers in Astronomy and Space Sciences, 7, 38

Mapelli, M. 2021, in Handbook of Gravitational Wave Astronomy, 4

Peters, P. C. 1964, Physical Review, 136, 1224

Peterson, C. J. & King, I. R. 1975, AJ, 80, 427

Portegies Zwart, S. F. & McMillan, S. L. W. 2000, ApJL, 528, L17

Rastello, S., Mapelli, M., Di Carlo, U. N., et al. 2021, MNRAS, 507, 3612

Rodriguez, C. L., Chatterjee, S., & Rasio, F. A. 2016, PRD, 93, 084029

Rodriguez, C. L., Morscher, M., Pattabiraman, B., et al. 2015, , 115, 051101

Spitzer, Lyman, J. & Harm, R. 1958, ApJ, 127, 544

Spitzer, L. 1987, Dynamical evolution of globular clusters

Stodolkiewicz, J. S. 1986, Acta Astronomica, 36, 19

Trani, A. A., Rastello, S., Di Carlo, U. N., et al. 2022, MNRAS, 511, 1362

Wang, L., Spurzem, R., Aarseth, S., et al. 2016, MNRAS, 458, 1450

Ye, C. S., Fong, W.-f., Kremer, K., et al. 2020, ApJ, 888, L10

Appendix A

Example Code

Below is a short example of a code that was used to extract information for escaping binary BHs from the simulated cluster models. Global properties for the cluster at the time of escape of each binary were also extracted.

```
import os
import sys
from subprocess import*
from string import *
import re
import math
import numpy as np
import json

# ----- CONSTANTS IN SI UNITS -----
c = 299792458
G = 6.67408e-11
Msun = 1.98847e30    # kg
Rsun = 6.95700e8    # m

# ----- SETTING THINGS UP -----
rootDir = '/work/mocca/acsomor/workspace/survey2/'

awk_escape_compact = '''awk '{if (NR>141 && ($17==14 && $18==14) && $26 != "")
                     print $1, $2, $3, $4, $5, $6, $7, $8, $9, $10,
                     $11, $12, $13, $14, $15, $16, $17, $18, $19, $20,
                     $21, $22, $23, $24, $25, $26}' escape.dat'''

outfile = open("escapers-BIG-onlyBBH.dat", 'w')

identifier = 0
```

```
# ----- LOOPING -----
for dirName, subdirList, fileList in os.walk(rootDir):
    os.chdir(dirName)
    if 'escape.dat' in fileList:
        pipe_esc_compact = Popen(awk_escape_compact, shell=True, stdout=PIPE,
                                 executable='/bin/bash').stdout
        output = pipe_esc_compact.read()
        if output != "":
            identifier = identifier+1
            output = output.splitlines()
            print(identifier, "   ", dirName)
            for line in output:
                time, tphys, im, id1, id2, iekind, ietype, escmas1, escmas2,
                escsemi, escecc, escdis, escene, escang, esctim, outputId,
                ik1, ik2, lastOutId, nkick, lastInterOutId, timenr, pop1,
                pop2, hist1, hist2 = line.split()

                # ----- MASS RATIO -----
                escmas1 = float(escmas1)
                escmas2 = float(escmas2)

                if escmas1 > escmas2:
                    m1 = escmas1
                    m2 = escmas2
                else:
                    m1 = escmas2
                    m2 = escmas1

                mass_ratio = m2/m1

                # ----- CHIRP MASS -----
                chirp_mass = ((m1*m2)**(3/5))*((m1+m2)**(-1/5))

                # ----- VELOCITY OF ESCAPER -----
                escene = float(escene)
                m_tot = m1 + m2
                esc_velocity = np.sqrt((np.abs(2*escene))/m_tot)


                # ----- MERGER TIME AND DELAY TIME -----
                tphys = float(tphys)
                escsemi = float(escsemi)
                escecc = float(escecc)
```

```
converter = 1/((60*60*24*365)*(10**6))
a = escsemi*Rsun
e = escecc
M1 = m1*Msun
M2 = m2*Msun

t_GW = (5/256)*((c**5 * a**4 * (1-e**2)**(7/2))/
        (G**3 * M1 * M2 *(M1 + M2)))*converter

t_delay = t_GW + tphys

# ----- SYSTEM FILE -----
awk_system = '''awk '{if (NR > 2327 && $2 >= '''+str(tphys)+''')
             print $2, $3, $14, $15, $16, $17, $18, $19, $20,
             $21, $22, $24, $26, $27, $28, $30, $32, $34,
             $35, $48, $52, $53, $55, $70, $72, $73, $74,
             $75, $76, $78, $79, $81, $82, $83, $84, $86,
             $87, $103, $129, $130, $131, $132, $134, $135,
             $142, $143, $152, $153, $154, $155, $156, $157,
             $158, $159, $160, $161, $162, $163, $164, $165,
             $166, $167, $170, $172, $173, $174, $175, $185,
             $186, $187, $188, $189, $190, $191, $192, $193,
             $194, $195, $196, $197, $198, $199, $200, $201,
             $202,  $203, $287, $288, $289, $290, $291, $292,
             $293}' system.dat | head -1 '''

pipe_system = Popen(awk_system, shell=True, stdout=PIPE,
                    executable='/bin/bash').stdout

output_system = pipe_system.read()
if output_system != "":
    output_system = output_system.splitlines()
    for line_esc in output_system:
        tphys_system, smt, rchut2, rcob, r10, r_h, rhob,
        rh2d, r70, rtid, xrc, vc, roc, rohut, u1, sbhm,
        ssbhm, csb, ppmax, nt, nbb, nescst, escns, ncoll,
        nb3b3, nescb3, nesb3s, ndist3, ndist4, nmerg3,
        nmerg4, idestr, imerge, ibiesc, ibirel, nexchang,
        nexchang2, nbss, ikickt, ikicktbs, ikicktbd,
        ikicktbm, ntsn1, ntsn2, lns, lbh, lot, l2wd, l2ns,
        l2bh, lmsms, lwdms, lwdns, iwdbh, lwdot, lnsms,
        lnsbh, lnsot, lbhms, lbhot, ldgdg, ldgot, lbh2, xms,
```

```
                    xwd, xns, xbh, xmsms, xwdwd, xnsns, xbhbh, xwdms,
                    xwdns, xwdbh, xwdot, xnsms, xnsbh, xnsot, xbhms,
                    xbhot, xdgdg, xdgot, xmsot, xotot, nbinrc,
                    nbinrchut2, smbh, kbh, rbh210, rbh250, rbh270, smbh2,
                    kbh2 = line_esc.split()


                # ----- REMOVE SPACES FROM PATHS TO DIRECTORIES-----
                def removeSpaces(string):
                    string = string.replace(' ','')
                    return string

                dirName_nospace = removeSpaces(dirName)

                # ----- WRITE OUTFILE -----
                outfile.write(str(line.decode('utf-8').strip()) + " " +
                              str(line_esc.decode('utf-8').strip()) + " " +
                              str(esc_velocity) + " " + str(m1) + " " +
                              str(m2) + " " + str(m_tot) + " " +
                              str(mass_ratio) + " " + str(chirp_mass) + " " +
                              str(t_GW) + " " + str(t_delay) + " " +
                              str(identifier) + " " + str(dirName_nospace) +
                              '\n')

outfile.close()
```